ESTIMATING FRACTURE DENSITY IN OCEANIC BASEMENT: AN APPROACH USING STONELEY WAVE ANALYSIS[1]

Marion Pfender[2, 3] and Heinrich W. Villinger[2]

ABSTRACT

We describe here our results using Stoneley waves as an indicator of fracture density in crystalline oceanic basement. During Ocean Drilling Program (ODP) Leg 205, ~170 m of oceanic crust was drilled and logged at Site 1253 in order to identify permeable fluid pathways in the downgoing plate of the Costa Rica subduction zone. Logging comprised the Dipole Shear Sonic tool for acoustic full waveform measurements including compressional, shear, and Stoneley waves.

We analyzed Stoneley waves, which have velocity and energy content that is inversely correlated to permeability, with a semblance algorithm in order to yield velocity and energy distribution. Our results are in very good agreement with ODP-processed Stoneley velocities in the igneous section of Site 1253, and in addition they yield an energy estimate.

In general, the observed velocity and energy loss correlates with zones of borehole breakouts, as predicted by theory. We concentrated on uniform borehole sections where we assume that data are only minimally influenced by geometry and changes in Stoneley wave properties are mainly induced by permeability. By considering fracture abundance obtained from both logging (Formation MicroScanner) and core observations, we found a correlation between increased fracture density and energy losses in these smooth borehole sections. Higher permeability might exist at 468, 492, 500, 508, and 518 meters below seafloor in the lower gabbro. We suggest that fluid flow in the oceanic basement of Site 1253 most likely occurs in these regions.

[2] Department of Geosciences, University of Bremen, PO Box 330440, D-28334 Bremen, Germany.
[3] BGR, Stilleweg 2, D-30655, Hannover, Germany.
pfender@soultz.net

INTRODUCTION

The oceanic crust formed at the East Pacific Rise (EPR) and subducted offshore Costa Rica (Fig. F1) has an anomalously low heat flow of only one-third of the expected value (Fisher et al., 2003). This is explained by fluid circulation in the basement of the downgoing plate, which effectively cools the crust (Kimura, Silver, Blum, et al., 1997).

How and where this fluid flow takes place was one focus of Ocean Drilling Program (ODP) Leg 205. Therefore, a ~170-m-thick interval of oceanic crust was cored and logged at Site 1253, ~200 m seaward of the Middle American Trench (MAT; Figs. F1, F2). Logging comprised density, porosity, and resistivity measurements (Shipboard Scientific Party, 2003c), Formation MicroScanner (FMS) electrical imaging of the borehole walls, and Dipole Shear Sonic (DSI) measurements. DSI records allow for full waveform processing of compressional (*P*-wave), head (*S*-wave), and Stoneley waves.

Stoneley waves are a useful indicator for possible fluid pathways because permeability increases their attenuation and decreases their velocity. Our research was intended to validate the usefulness of such DSI logs for assessment of hydrological properties of oceanic basement rocks. If possible, we aimed to derive a qualitative permeability estimate from Stoneley waves in crystalline basement at Site 1253. A quantitative analysis is beyond the scope of this paper because it would require comparison with in situ permeabilities not yet available from circulation obviation retrofit kit (CORK) data or a sophisticated inversion technique (i.e., Brie et al., 2000).

Based on a database search (**iodp.tamu.edu/publications/citations/ database.html**), it seems that not many studies have been performed on Stoneley wave data collected during ODP, although full waveform acoustic logging has been performed as a standard for several years. In contrast, the exploration industry uses Stoneley wave attenuation to detect and characterize permeable zones based on hydrocarbon production (Mikhailov et al., 2000; Hornby et al., 1989). Their main interest, however, is focused mainly on boreholes in sedimentary rocks.

It is therefore sensible to evaluate whether processing Stoneley waves recorded in crystalline basement boreholes yields additional information on permeability distribution. This information could complement core measurements and other methods to derive permeability and could be of special interest in boreholes where core recovery is small. Our research could indicate that Stoneley wave processing could be implemented into standard ODP data processing to add information without requiring more measurement time.

In this paper, we present our attempts to use Stoneley waves to identify permeable zones in the basement logged at Site 1253. In order to derive their velocity and energy profiles with depth, we applied a semblance analysis to detect coherent arrivals in the full waveform records. Although velocity was already a result of onboard processing by the Schlumberger engineers and helped us in controlling the performance of our algorithm, Stoneley energy is not derived in standard ODP processing. We identified zones of higher attenuation and lower velocity in the profiles, but this effect can be also induced by borehole breakouts. Therefore, we restricted our further investigations to smooth borehole sections, assuming that the observed velocity and energy variations are mainly permeability induced in those sections. We then correlated Stoneley wave attenuation with core and FMS fracture observations.

F1. Costa Rica drilling area and isochrons, p. 12.
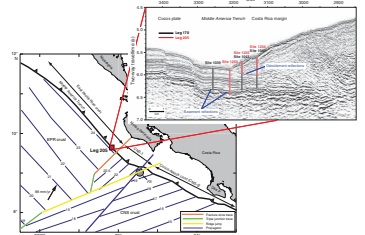
F2. Logging data and physical property measurements, p. 13.
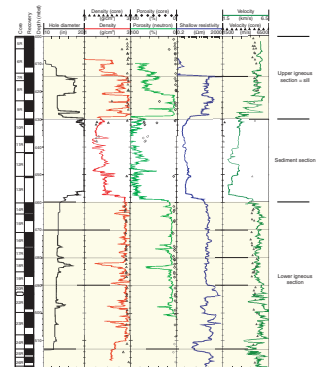
We will present an overview of acoustic logging and then introduce the Stoneley wave. A short description of the semblance analysis concept will be given before we present calculated velocities and energy estimates for Stoneley waves. Finally, we will discuss the results, including FMS measurements and fracture observation on cores.

GEOLOGICAL SETTING AND BACKGROUND

The Costa Rica convergent margin is formed by subduction of the Cocos plate beneath the Carribean plate off Costa Rica (Fig. F1). The subducted oceanic crust, created at the East Pacific Rise (EPR), is anomalously cold with a mean heat flow ~30 mW/m² in contrast to the expected value of 90–120 mW/m² for its crustal age of 20–24 Ma (Fisher et al., 2003). This is interpreted to be the result of hydrothermal circulation in exceptionally highly permeable upper oceanic crust, which effectively removes heat from the incoming plate (Fisher et al., 2003). This hypothesis is supported by geochemical pore water investigations on sediments recovered from an interval just above the sediment/basement interface at Site 1039 (ODP Leg 170) that suggests fluid flow of near-seawater composition below the sediments (Kimura, Silver, Blum, et al., 1997). Both the heat flow anomaly and pore fluid profiles have been modeled in terms of active fluid flow at rates of ~1 m/yr (Silver et al., 2000), having residence time of at least ~15,000 yr.

How and where this fluid flow takes place in the downgoing oceanic crust was one focus of Leg 205 (Fig. F1). Building on Leg 170, this leg was designed to investigate the igneous and alteration history of the downgoing plate and the hydrological activity across the Costa Rica margin. All Leg 205 (Sites 1253, 1254, and 1255) and Leg 170 (Sites 1039, 1040, and 1043) drill sites are located on one multichannel seismic profile (Fig. F1) that shows the structure of the subduction zone. At Sites 1039 and 1253, a 400-m-thick sequence of sediments overlays a gabbro sill as documented in cores from Site 1039 (Leg 170; Kimura, Silver, Blum, et al., 1997). It forms the strong reflector in the seismic section (Fig. F1) at 6.34 s two-way traveltime (TWT) and makes the top of oceanic basement below very difficult to identify.

Science objectives specific to reference Site 1253, located ~200 m seaward of the MAT (Fig. F1), center on mass flux to the subduction zone (and ultimately the volcanic arc) as well as the permeability, thermal structure, and hydrology of the downgoing igneous section. These goals were accomplished by coring, downhole temperature and pressure measurements, and logging (Shipboard Scientific Party, 2003a). A long-term pressure and temperature observatory CORK-II (Jannasch et al., 2003) with temperature probes and two osmotic fluid and gas samplers was installed in the basement; results are described in Heesemann et al., this volume, and Davis and Villinger (2006).

At Site 1253 on the incoming plate, we cored 230 m, including ~170 m within two igneous units. The upper unit extends from 400 to 430 mbsf and is a gabbro sill with sediments above and below (Fig. F2). It is comparable to similar units cored at Leg 170 Holes 1039B and 1039C (Kimura, Silver, Blum, et al., 1997), which form the strong reflector in the seismic image in Figure F1. The second, lower igneous unit was drilled from 460 to 600 mbsf and is more extensively altered below 510–513 mbsf. Logging in these formations (Fig. F2) consisted of one run with the triple combination tool string (triple combo; Shipboard Scientific Party, 2003c), comprising density, porosity, and resistivity

measurements, and two runs with the FMS-sonic tool string: the FMS for an electrical imaging of the borehole walls and the DSI tool for sonic measurements. DSI records allow for full waveform processing of *P*-waves, *S*-waves, and Stoneley waves.

METHOD: AQUISTION AND PROCESSING OF ACOUSTIC WAVES IN BOREHOLES

In this section we describe basic features of acoustic wave propagation in boreholes and introduce characteristics of the Stoneley wave. The standard data processing to derive wave velocity as well as our additional processing to yield energy content is explained.

Wave Propagation in Boreholes

In a borehole, an acoustic source pulse disintegrates into a number of discrete mode peaks with successively increasing frequencies (Paillet and Cheng, 1991) and generates complicated interference patterns. Classical theory predicts a full wave train consisting of a head *P*-wave, a head *S*-wave, guided waves including a number of normal modes, and a Stoneley wave (Chen, 1982). Their features are summarized in Table **T1;** a detailed description of the great number of complex wave types generated in boreholes can be found in Paillet and Cheng (1991, 1986) and Paillet and White (1982).

We focus on the Stoneley wave, which is the fundamental mode of guided waves (Winkler et al., 1989; Paillet and Cheng, 1991). Its wave motion is an expanding/contracting borehole motion (Qobi et al., 2001), illustrated in Figure **F3.** The radial component of the Stoneley wave forces fluid into fractures, which results in a loss of energy (i.e., decrease of amplitude), and this effect is responsible for the sensitivity of Stoneley waves to permeability.

## Effects of Permeability on Stoneley Wave Propagation

Stoneley waves are not directly affected by permeability (κ) but by mobility (*m*), which is the ratio of permeability to fluid viscosity (μ) (Qobi et al., 2001; Brie et al., 2000). In general, μ is known and more or less constant within one borehole so that *m* can be taken as a proxy for κ.

Permeability can influence Stoneley wave propagation in three ways. Stoneley waves can be partly reflected at sharp impedance contrasts (Gelinsky et al., 1998; Brie et al., 2000) such as fractures, lithology, or borehole diameter changes. Moreover, as formation permeability increases, Stoneley wave velocity decreases (Winkler et al., 1989), thereby inducing dispersion. The third effect is the attenuation of Stoneley waves, which we investigate in this paper.

Attenuation occurs when fluid is pressed into the permeable formation and energy is lost in the relative motion between viscous pore fluid and the elastic solid matrix (Norris, 1989). Attenuation therefore correlates with permeability, but unfortunately, lithologic boundaries or variable borehole geometry also attenuate Stoneley waves (Paillet and White, 1982). Consideration of other logging and core measurements is necessary to distinguish between the possible causes of the observed attenuation. Modeling the geometric effect is essential for a quantitative
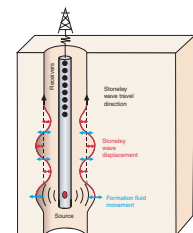
meaningful interpretation but is of minor importance if only qualitative changes of downhole permeability are derived.

Acoustic Logging Tool

The DSI tool is a full waveform acoustic logging tool that delivers measurements of sonic wave propagation in a wide variety of formations (Shipboard Scientific Party, 2003c). This tool, illustrated in Figure F4, consists of a linear array of eight receiver stations spaced 15.24 cm (6 in) apart and two different transmitters (Lamont-Doherty Earth Observatory–Borehole Research Group Wireline Logging Services Guide [LDEO-BRG, 2000]). The monopole transmitter with an omnidirectional source characteristic generates a high-frequency pulse (~14 kHz, called P&S mode) for *P* and *S* head waves and a low-frequency pulse (~1 kHz, called Stoneley mode) for Stoneley wave excitation. The two dipole transmitters that create nonaxisymmetric signals drive a low-frequency pulse (~2 kHz) for flexural wave excitation, which is normally used to estimate shear wave velocity in highly unconsolidated formations. Each receiver station contains two hydrophone pairs oriented perpendicular to each other and parallel to the upper and lower dipole transmitter.

In the acquisition cartridge, the waveforms undergo automatic gain control and are digitized (12-bit dynamic range). A 40-μs sampling interval is used for the low-frequency Stoneley and all dipole modes and 10 μs for the higher frequency P&S mode. Each record consists of 512 samples, resulting in a record length of ~20 ms for Stoneley waves and ~5 ms for *P*- and *S*-waves.

Postprocessing of Acoustic Records

Standard processing of acoustic records comprises a waveform correlation of the digital signals to find coherent arrivals across the receiver array. Waveform correlation consists of an analysis of semblance, which is a measure of correlation between waveforms that takes into account both signal shape and amplitude and which is used to find coherent arrivals of a wave traveling in a medium (i.e., Taner and Koehler, 1969; Kimball and Marzetta, 1984). It is a function of arrival time at near-receiver and acoustic wave velocity and ranges between 0 for noncorrelated signals and 1 for perfectly correlated waveforms. Standard processing calculates semblance for all sensible combinations of arrival time and wave velocity and identifies local maxima of semblance in the following picking and labeling process. The corresponding velocity and energy are stored, and the procedure is repeated for each source shot to create velocity and energy depth profiles.

The routine processing of DSI data onboard the *JOIDES Resolution* is performed by the engineer on a Schlumberger MAXIS system, and final processing is done on GeoFrame at LDEO (Shipboard Scientific Party, 2003c). This processing comprises a waveform correlation (slowness time coherence [STC]) providing the acoustic wave velocities (V_P, V_S, and $V_{Stonely}$) that are then available in the database. However, the energy content of the identified waves was not available for the Leg 205 data.

Because our research focused on the analysis of Stoneley wave attenuation, we subjected the Stoneley waveform data to semblance analysis to yield energy estimates. We used the algorithm reported in Kimball and Marzetta (1984) and implemented it in Matlab, extended by the capability to store arrival time and to calculate the energy contained in
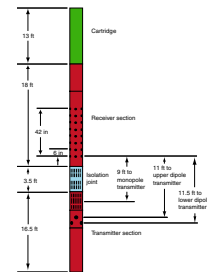
the detected arrival. Again following Kimball and Marzetta (1984), we considered as an energy estimate the power in the trace stacked with the identified wave velocity. Tests on synthetic data overlain with random noise have proven that the algorithm identifies arrivals with the accuracy in the range of the algorithm's velocity resolution.

RAW DATA AND RESULTS

Site 1253 was logged from 564 mbsf up to 413 mbsf with 1272 shots and a vertical resolution of 6 in corresponding to the receiver spacing. We present acoustic data from ~80 m of the lower igneous section, 30 m of sediment above it, and 17 m of the sill (Fig. F2). We show records of monopole modes (P&S and Stoneley) and concentrate on the results of semblance processing for the Stoneley wave in the lower igneous section.

Influence of Borehole Diameter on Waveform Records

Borehole geometry, essential for the interpretation of acoustic data, was determined using caliper data from one run of the triple combo logging string and two passes of the FMS-sonic tool string. Because only two opposing hydraulic arms out of four on the FMS tool worked, the second logging pass had a 90° rotation from the orientation of the first pass, thus providing a more complete picture of the borehole shape. Figure F5 shows the caliper measurements that reveal the boundaries from 10¾ in casing to the 14¾ in open hole at 413 mbsf and the narrowing to a $9^7/_8$ in hole at 423 mbsf. The sediment section from 430 to 460 mbsf is strongly washed out, so the caliper arms lost wall contact. The borehole has some smooth intervals in the lower igneous section, such as the one at ~465–475 mbsf, but generally shows numerous breakouts ranging up to 4 in. Figure F5 indicates that caliper measurements could not be unambiguously reproduced in the three runs (for example, in the breakout zone at 510 mbsf). The borehole seems to have a complex shape with changing ellipticity, which complicates Stoneley wave interpretation and influences acoustic data recorded in P&S and Stoneley modes. These so-called iso-offset sections (Fig. F5) show the full waveform records of one specific receiver (here the near receiver) with depth.

In P&S mode, data quality is generally good (Fig. F5, left); the first arrivals, the *P* head waves, are clearly visible and mimic borehole geometry. The *S*-wave, following the *P*-wave, cannot be identified in this illustration. The direct fluid wave is the strong onset at 1.8 ms. Arrivals are delayed, such as in the breakout zone at ~510–515 mbsf. A series of enlargements measured from 525 to 535 mbsf is only poorly portrayed in acoustic data records, and we suspect that they are disturbed by the strongly varying diameter or by a nonconstant tool movement.

Acoustic data recorded in Stoneley mode (Fig. F5, right) show a broad band of Stoneley amplitudes at ~2 ms but also a higher amount of noise. In the sediment section, the Stoneley arrival is strongly distorted, and perhaps the Stoneley mode could not develop. As in the P&S mode, Stoneley waveforms are displaced and disturbed by borehole irregularities at 510–515 and 525–535 mbsf.
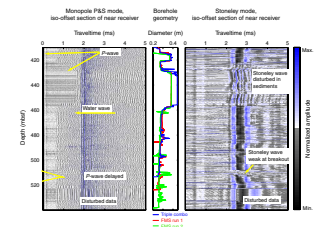
Compressional and Shear Velocities

After bandpass filtering following Harrison et al. (1990), we calculated velocities and energies from raw unnormalized data. The parameters used in our semblance analysis are summarized in Table T2 for P&S and Stoneley modes.

S-wave velocities (Fig. F6) differ from ODP results even in a smooth section at ~465–475 mbsf, although data quality is good. Part of the deviation is explained by the fact that the shipboard processing calculated *S*-wave velocities from dipole measurements while we processed the monopole data. Dipole mode is usually only used in unconsolidated formations to derive *S*-wave velocity. Another explanation might simply be that our algorithm "sticks" at one semblance maximum at the lowest limit of velocity, which is water velocity. This occurs, for example, from 410 to 460 and 490 to 510 mbsf.

In contrast, the picked *P*-wave velocities agree well throughout the profile, with the exception of the sediment section and from 495 to 510 mbsf. In the sediment section, *P*-waves might be difficult to pick because of geometric disturbances (cf. Fig. F5). We suspect that from 495 to 510 mbsf, the algorithm picks the *S*-wave instead of the *P*-wave in the labeling process. However, good correlation in a great part of the borehole indicates that our algorithm works reliably.

Stoneley Velocity and Energy Estimates

Stoneley wave data quality was significantly improved by bandpass filtering, and our processing yields almost exactly the shipboard velocities in the majority of the logged igneous sections. Figure F7 shows that, from 460 to 490 mbsf, deviations between the two data sets are mainly <20 m/s and increase to 40 m/s below 490 mbsf. Greater differences in Stoneley wave velocities are in the wide sediment section, where hole conditions and data quality are obviously bad. Figure F7 also shows the loss of energy in decibels compared to the location of highest energy in the profile which is at 405 mbsf in the cased section. Without the possibility of comparing our results to the output of different processing methods, it is difficult to estimate the reliability of these data. However, because the variations in energy correlate, as expected, with variations in velocity (which were shown to be consistent with shipboard results), we assume a similar robust result.

Both energy and velocity variations correlate inversely with borehole diameter. The trend shows higher velocity and energy in smooth and narrow borehole sections, such as the one at ~465 mbsf, and lower velocity and energy in wider sections or breakout zones, such as the one at ~495 mbsf.

This correlation agrees with our theory but prohibits a clear identification of possible permeable zones. Because geometry and permeability can both attenuate and slow Stoneley waves, an interpretation of permeability distribution from these measurements alone is not possible. For this reason, we concentrate our discussion below on smooth borehole sections and assume that geometric effects therein are minimal. Figure F8 is a compilation of borehole diameter, Stoneley velocity, and energy from 460 to 540 mbsf and shows the smooth borehole sections marked by the light blue shading. These five zones are all within the lower igneous unit; the washed-out sediment section and the irregular borehole in the sill are not taken into account for further discussion.
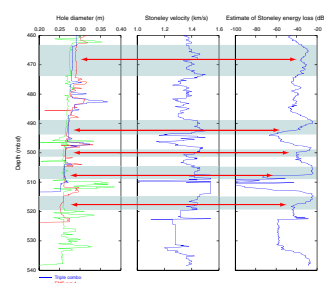
T2. Velocity and amplitude calculations, p. 22.

F6. Borehole diameter and *S*- and *P*-wave velocity, p. 17.
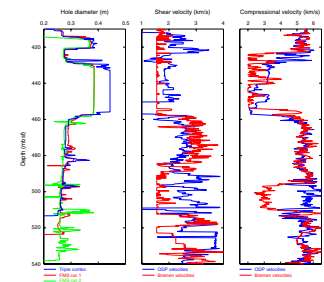
F7. ODP vs. Bremen measurements, p. 18.
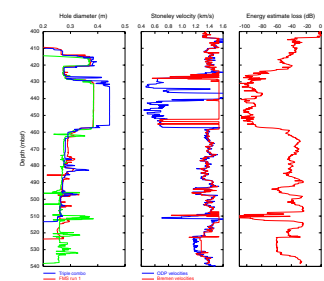
F8. Borehole diameter, Stoneley wave velocity, and Stoneley energy, p. 19.

DISCUSSION

The following discussion concentrates on five smooth zones within the lower igneous unit. We assume that geometry influence is minimal in these regions, so local energy and velocity minima occurring within these zones can be regarded as mainly permeability induced.

Figure F8 shows borehole diameter together with Stoneley velocity and energy from 460 to 540 mbsf and highlights smooth borehole sections with blue shading. In spite of the uniform borehole geometry, we observe local minima of velocity and energy at 468, 492, 500, 508, and 518 mbsf (red arrows). We suppose that permeability changes occur at those locations and therefore correlate our observations to fracture observations on FMS images and core samples in the next section.

Stoneley Waves and Fractures

To test the hypothesis of nongeometry-induced energy variations in smooth borehole sections, we take a close look at fracture abundance in the above defined regions. Fractures were observed during Leg 205 on the recovered core material by a thorough visual inspection (Shipboard Scientific Party, 2003b) and interpretation of FMS logging data.

These data sets are compiled in Figure F9 together with borehole diameter and energy changes. Logging data from the FMS tool complement core investigations in areas of a low recovery, such as at 466–470 mbsf, where the common ODP curation practice attributes the whole recovered core material to the top of the cored section.

We found that, in contrast to our first expectations, breakout zones do not show significantly more fractures than smooth zones. Only a small increase in number of fractures with depth is noted, which might fit the observation that the lower igneous unit is more fractured below 514 mbsf.

Energy losses within smooth borehole intervals are again marked with red arrows in Figure F9 and might be linked to a locally increased fracture abundance in those intervals. At the uppermost level, 468 mbsf, the number of fractures from the FMS is at its locally maximal value of four fractures per meter. The local maximum in fractures observed on core material occurs at shallower depths from 464 to 466 mbsf. This difference might arise from low core recovery and the curation practice. Slightly below 490 mbsf, in the vicinity of the second energy minimum, we find a local high in fracture abundance on core material and a rising number from FMS observation. This correlation is much clearer at 500 mbsf where both observations show a high fracture abundance in a smooth borehole section. At 508 mbsf, the energy decrease might be tied to the maximum in fracture number from FMS data. The last of the five smooth zones shows minimal energy at ~518 mbsf, which coincides very well to the overall maximal fracture number in the FMS data and the relative high abundance of fractures in core observations.

Within each of the five sections of uniform borehole geometry, we can assign an increased number of fractures, observed on FMS images and on cores, to a minimum in Stoneley wave energy. Unfortunately, a further correlation of these observations with petrophysical findings, such as subsections of the lower igneous unit or degree of alteration, is not possible. Our analysis is much too limited to the smooth zones for

F9. Core recovery, fractures, Stoneley energy, and borehole diameter, p. 20.
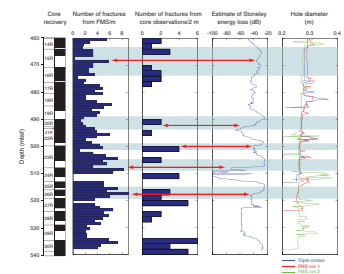
such a purpose and prohibits a detailed comparison to the whole logged igneous section.

CONCLUSIONS

Our aim was to qualitatively infer fracture density of oceanic crystalline basement from full waveform acoustic logging data from Site 1253, Leg 205, and from that to validate the usefulness of DSI logs for assessing hydrological properties of oceanic basement rocks.

For this purpose, we processed the Stoneley wave for velocity and energy content by deploying a straightforward semblance algorithm. We observed a correlation between borehole geometry and Stoneley wave energy and velocity, as expected. Our further interpretations therefore concentrated on five smooth borehole sections in order to minimize the geometry effect. Combination with fracture observations performed downhole and on recovered core material linked the local low-energy locations to local maxima in fracture abundance. We identified five zones at depths of 468, 492, 500, 508, and 518 mbsf as probably being of higher permeability.

A quantitative permeability estimate is not possible with our processing, and the qualitative investigation reported here also requires, at the current state, comparison with other fracture observations such as core or FMS measurements.

An improvement of our algorithm would be possible by comparing it with Stoneley wave energy distribution calculated by the Geoframe software. We also suggest modeling the influence of borehole geometry on Stoneley velocity and energy and implementing such a model in Matlab. More precise diameter information would be helpful, as well as an extended and undisturbed borehole section for measurements and comparison.

Nevertheless, we have shown that the Stoneley wave energy distribution delivers additional information to the standard data curation process for crystalline rocks. This is especially interesting in cases where no cores could be recovered. The possibility of calculating Stoneley wave energy distribution is included in the Geoframe software, and it would be worth, for future research, to make use of this possibility, especially because recording Stoneley waves is already a standard and does not require additional time.

ACKNOWLEDGMENTS

REFERENCES

Barckhausen, U., Ranero, C.R., von Huene, R., Cande, S.C., and Roeser, H.A., 2001. Revised tectonic boundaries in the Cocos plate off Costa Rica: implications for the segmentation of the convergent margin and for plate tectonic models. *J. Geophys. Res.,* 106(B9):19207–19220. doi:10.1029/2001JB000238

Brie, A., Endo, T., Johnson, D.L., and Pampuri, F., 2000. Quantitative formation permeability evaluation from Stoneley waves. *SPE Reservoir Eval. Eng.,* 3(2):109–117.

Chen, S.T., 1982. The full acoustic wave train in a laboratory model of a borehole. *Geophysics,* 47(11):1512–1520. doi:10.1190/1.1441301

Cheng, C.H., and Toksöz, M.N., 1981. Elastic wave propagation in a fluid-filled borehole and synthetic acoustic logs. *Geophysics,* 46(7):1042–1053. doi:10.1190/1.1441242 [AUTHOR: Please cite in paper or delete from list.]

Davis, E.E., and Villinger, H.W., 2006. Transient formation fluid pressures and temperatures in the Costa Rica forearc prism and subducting oceanic basement: CORK monitoring at ODP Sites 1253 and 1255. *Earth Planet. Sci. Lett.,* 245(1–2):232–244. doi:10.1016/j.epsl.2006.02.042

DeMets, C., Gordon, R.G., Argus, D.F., and Stein, S., 1990. Current plate motions. *Geophys. J. Int.,* 101:425–478.

Fisher, A.T., Stein, C.A., Harris, R.N., Wang, K., Silver, E.A., Pfender, M., Hutnak, M., Cherkaoui, A., Bodzin, R., and Villinger, H., 2003. Abrupt thermal transition reveals hydrothermal boundary and role of seamounts within the Cocos plate. *Geophys. Res. Lett.,* 30(11):1550–1553. doi:10.1029/2002GL016766

Gelinsky, S., Patterson, D., Tang, X., and Cheng, A., 1998. Anisotropic permeability in fractured reservoirs from integrated acoustic measurements. *SEG Tech. Program Expanded Abstr.,* 956–959. doi:10.1190/1.1820651

Harrison, A.R., Randall, C.J., Aron, J.B., Morris, C.F., Wignall, A.H., Dworak, R.A., Rutledge, L.L., and Perkins, J.L., 1990. Acquisition and analysis of sonic waveforms from a borehole monopole and dipole source for the determination of compressional and shear speeds and their relation to rock mechanical properties and surface seismic data. *SPE Soc. Pet. Eng. AIME,* 65:267–282.

Hearst, J.R., Nelson, P.H., and Paillet, F.L., 2001. *Well Logging for Physical Properties: A Handbook for Geophysicists, Geologists, and Engineers* (2nd ed.): New York (J. Wiley and Son). [AUTHOR: Please cite in paper or delete from list.]

Hornby, B.E., Johnson, D.L., Winkler, K.W., and Plumb, R.A., 1989. Fracture evaluation using reflected Stoneley wave arrivals. *Geophysics,* 54(10):1274–1288. doi:10.1190/1.1442587

Jannasch, H., Davis, E., Kastner, M., Morris, J., Pettigrew, T., Plant, J.N., Solomon, E., Villinger, H., and Wheat, C.G., 2003. CORK-II: long-term monitoring of fluid chemistry, fluxes, and hydrology in instrumented boreholes at the Costa Rica subduction zone. *In* Morris, J.D., Villinger, H.W., Klaus, A., *Proc. ODP, Init. Repts.,* 205, 1–36 [CD-ROM]. Available from: Ocean Drilling Program, Texas A&M University, College Station TX 77845-9547, USA. [HTML]

Kimball, C.V., and Marzetta, T.L., 1984. Semblance processing of borehole acoustic array data. *Geophysics,* 49(3):274–281. doi:10.1190/1.1441659

Kimura, G., Silver, E.A., Blum, P., et al., 1997. *Proc. ODP, Init. Repts.,* 170: College Station, TX (Ocean Drilling Program). [HTML]

Lamont-Doherty Earth Observatory–Borehole Research Group, 2000. *ODP Logging Manual: An Electronic Guide to ODP Logging Services,* Version 2.0, [CD-ROM]. Available from: Lamont-Doherty Earth Observatory, Columbia University, Palisades NY 10964, USA. [HTML]

Mikhailov, O.V., Queen, J., and Toksöz, M.N., 2000. Using borehole electroseismic measurements to detect and characterize fractured (permeable) zones. *Geophysics,* 65(4):1098–1112. doi:10.1190/1.1444803

Morris, J.D., Villinger, H.W., Klaus, A., et al., 2003. *Proc. ODP, Init. Repts.,* 205 [CD-ROM]. Available from: Ocean Drilling Program, Texas A&M University, College Station TX 77845-9547, USA. [HTML]

Norris, A.N., 1989. Stoneley wave attenuation and dispersion in permeable formations. *Geophysics,* 54(3):330–341. doi:10.1190/1.1442658

Paillet, F.L., and Cheng, C.H., 1986. A numerical investigation of head wave and leaky modes in fluid-filled boreholes. *Geophysics,* 51(7):1438–1449. doi:10.1190/1.1442192

Paillet, F.L., and Cheng, C.H., 1991. *Acoustic Waves in Boreholes:* Boca Raton, FL (CRC Press).

Paillet, F.L., and White, J.E., 1982. Acoustic modes of propagation in the borehole and their relationship to rock properties. *Geophysics,* 47(8):1215–1228. doi:10.1190/1.1441384

Qobi, L., de Kuijper, A., Tang, X.M., and Strauss, J., 2001. Permeability determination from Stoneley waves in the Ara group carbonates, Oman. *GeoArabia,* 6(4).

Shipboard Scientific Party, 2003a. Leg 205 summary. *In* Morris, J.D., Villinger, H.W., Klaus, A., *Proc. ODP, Init. Repts.,* 205, 1–75 [CD-ROM]. Available from: Ocean Drilling Program, Texas A&M University, College Station TX 77845-9547, USA. [HTML]

Shipboard Scientific Party, 2003b. Site 1253. *In* Morris, J.D., Villinger, H.W., Klaus, A., *Proc. ODP, Init. Repts.,* 205, 1–184 [CD-ROM]. Available from: Ocean Drilling Program, Texas A&M University, College Station TX 77845-9547, USA. [HTML]

Shipboard Scientific Party, 2003c. Explanatory notes. *In* Morris, J.D., Villinger, H.W., Klaus, A., *Proc. ODP, Init. Repts.,* 205, 1–76 [CD-ROM]. Available from: Ocean Drilling Program, Texas A&M University, College Station TX 77845-9547, USA. [HTML]

Silver, E., Kastner, M., Fisher, A., Morris, J., McIntosh, K., and Saffer, D., 2000. Fluid flow paths in the Middle America Trench and Costa Rica margin. *Geology,* 28(8):679–682.

Taner, M.T., and Koehler, F., 1969. Velocity spectra-digital derivation and applications of velocity functions. *Geophysics,* 34(6):859–881. doi:10.1190/1.144058

Winkler, K.W., Liu, H.-L., and Johnson, D.L., 1989. Permeability and borehole Stoneley waves: comparison between experiment and theory. *Geophysics,* 54(1):66–75. doi:10.1190/1.1442578

Figure F1. Leg 205 Costa Rica drilling area (red box) and isochrons derived from seafloor magnetic anomalies (Barckhausen et al., 2001). Numbers indicate crustal age in millions of years. Tectonic boundaries, convergence direction and rate (arrows; DeMets et al., 1990), and arc volcanoes (triangles) are shown. Drill sites of Leg 205 (red square) are located on crust generated at the East Pacific Rise (EPR), which converges with a rate of 88 mm/yr (DeMets et al., 1990) toward the Carribean plate. Inset is of seismic Profile BGR 99-44 (C. Reichert and C. Ranero, pers. comm., 2001) across the Middle American Trench. Sites 1039–1043 were drilled during Leg 170 (Kimura, Silver, Blum et al., 1997); Sites 1253–1255 (red) were added during Leg 205 (Morris, Villinger, Klaus, et al., 2003). At 6.34 s two-way traveltime, the basement reflection corresponding to the sill can be identified beneath the location of Site 1039 and 1253. CNS = Cocos-Nazca spreading center, FS = Fisher Seamount.
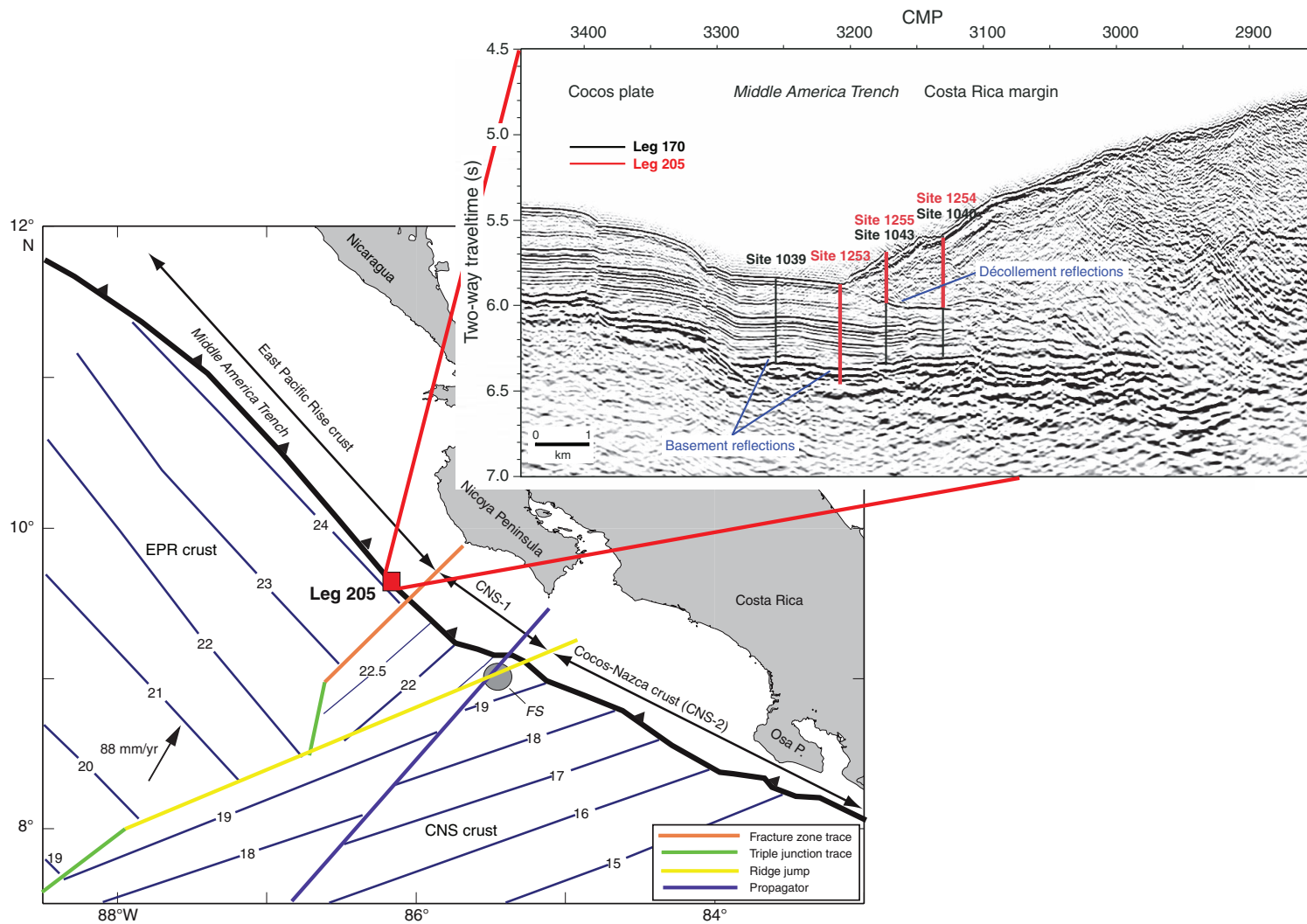
Figure F2. Compilation of logging data and physical property measurements at Site 1253 (Shipboard Scientific Party, 2003b). From left to right: core recovery, hole diameter (logged = black line), density (core = diamonds, logged = red line), porosity (core = diamonds, logged = green line), resistivity (logged = blue line) and compressional wave velocity (core = diamonds, logged = green line). The two igneous units (yellow shading) can be distinguished in all parameters from the intermittent sediment section. The lower igneous unit comprises several subunits, indicating different stages of alteration and an increase in fractures abundance at a depth below 513 mbsf. OsmoSamplers were installed at 500 and 515 mbsf.

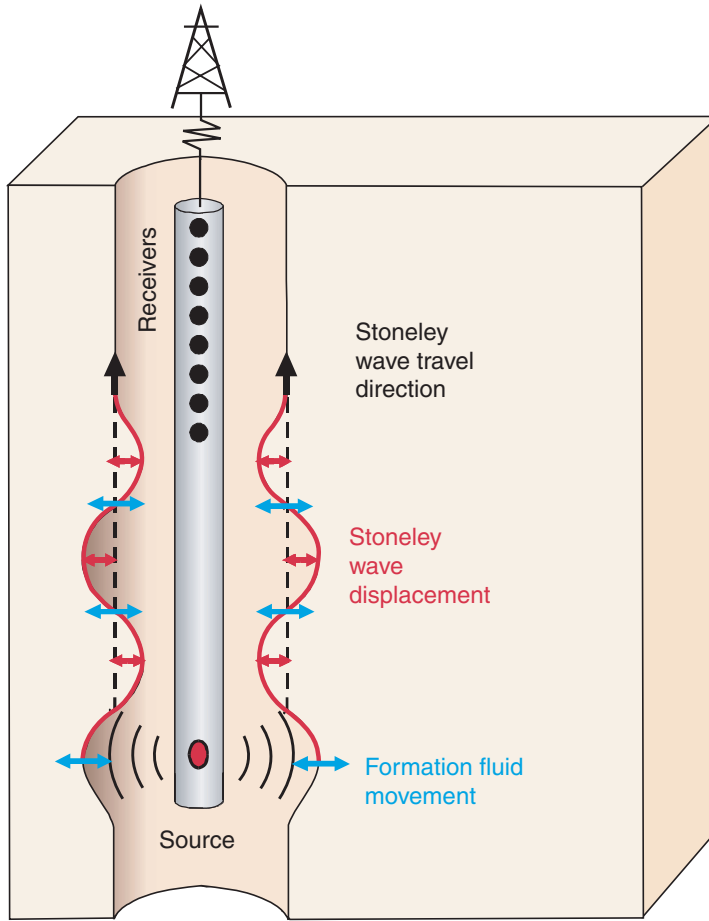**Figure F3.** Stoneley wave motion (figure after Qobi et al., 2001).

Figure F4. Dipole Shear Sonic tool (DSI) for acoustic logging (figure taken from Borehole Research Group), consisting of a transmitter section, an isolation joint, and a linear array of eight receivers (spacing = 6 in). Overall length = 15.5 m. A monopole source is driven in high and low frequencies for the generation of *P*- and *S*-waves and in a low frequency for Stoneley waves. The dipole excites flexural waves for *S*-wave velocity determination in soft formations.
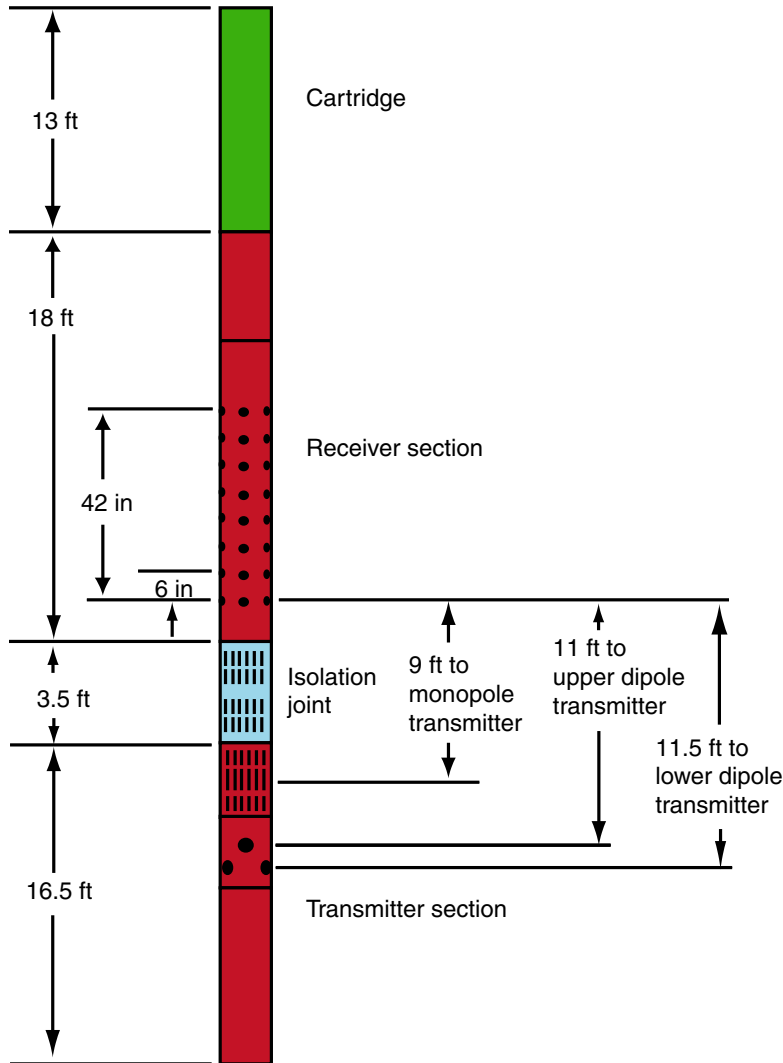
Figure F5. Iso-offset sections (all records of one receiver with depth) of monopole compressional and shear mode records and Stoneley mode records. Shot distance = 15.24 cm, timescale = 5 ms, and amplitudes are normalized. Borehole diameter as determined from the triple combo and Formation MicroScanner tool strings. Color scheme improves visibility of small amplitudes and polarity reversals.
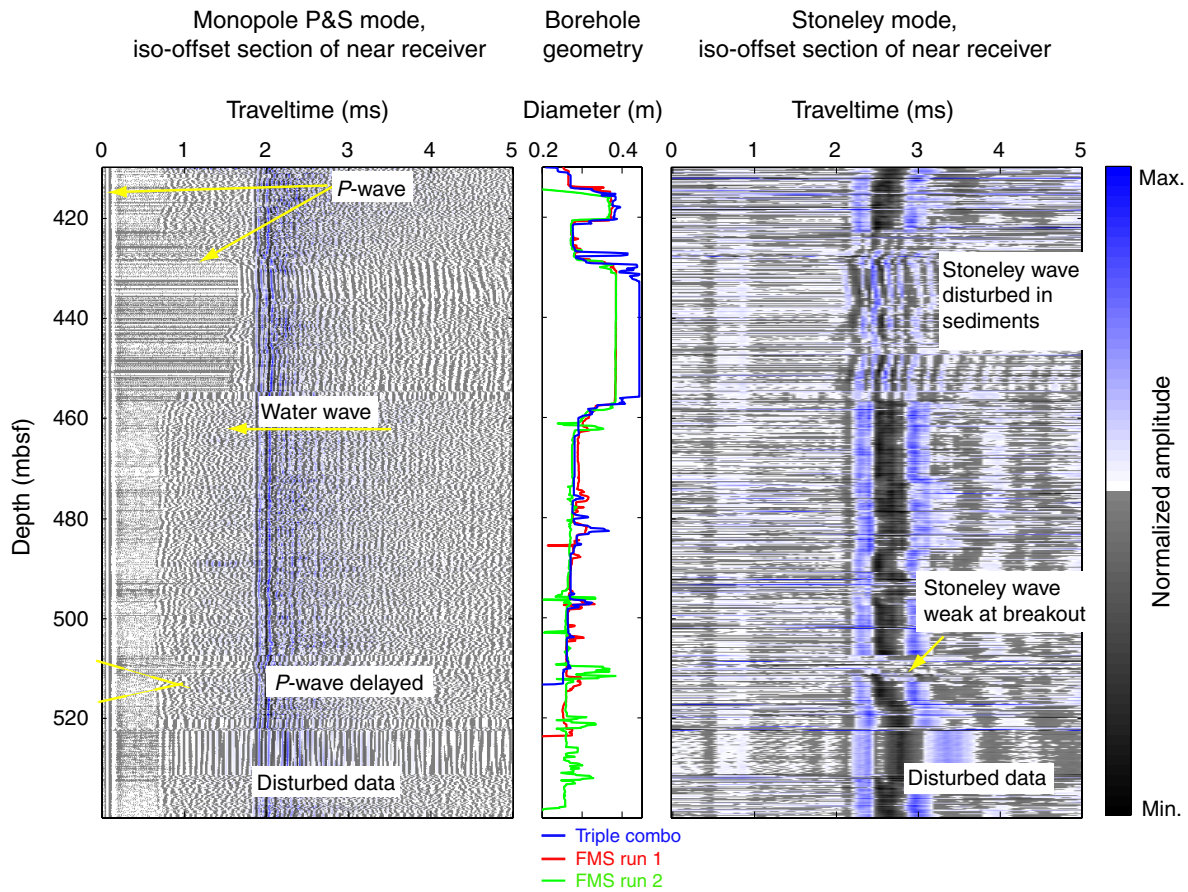
Figure F6. Borehole diameter measurements and picked *S*- and *P*-wave velocity (right). Differences in *S*-wave velocities are due to different data sets used during processing. For the *P*-wave, results are in good agreement except for the sediment section. FMS = Formation MicroScanner.
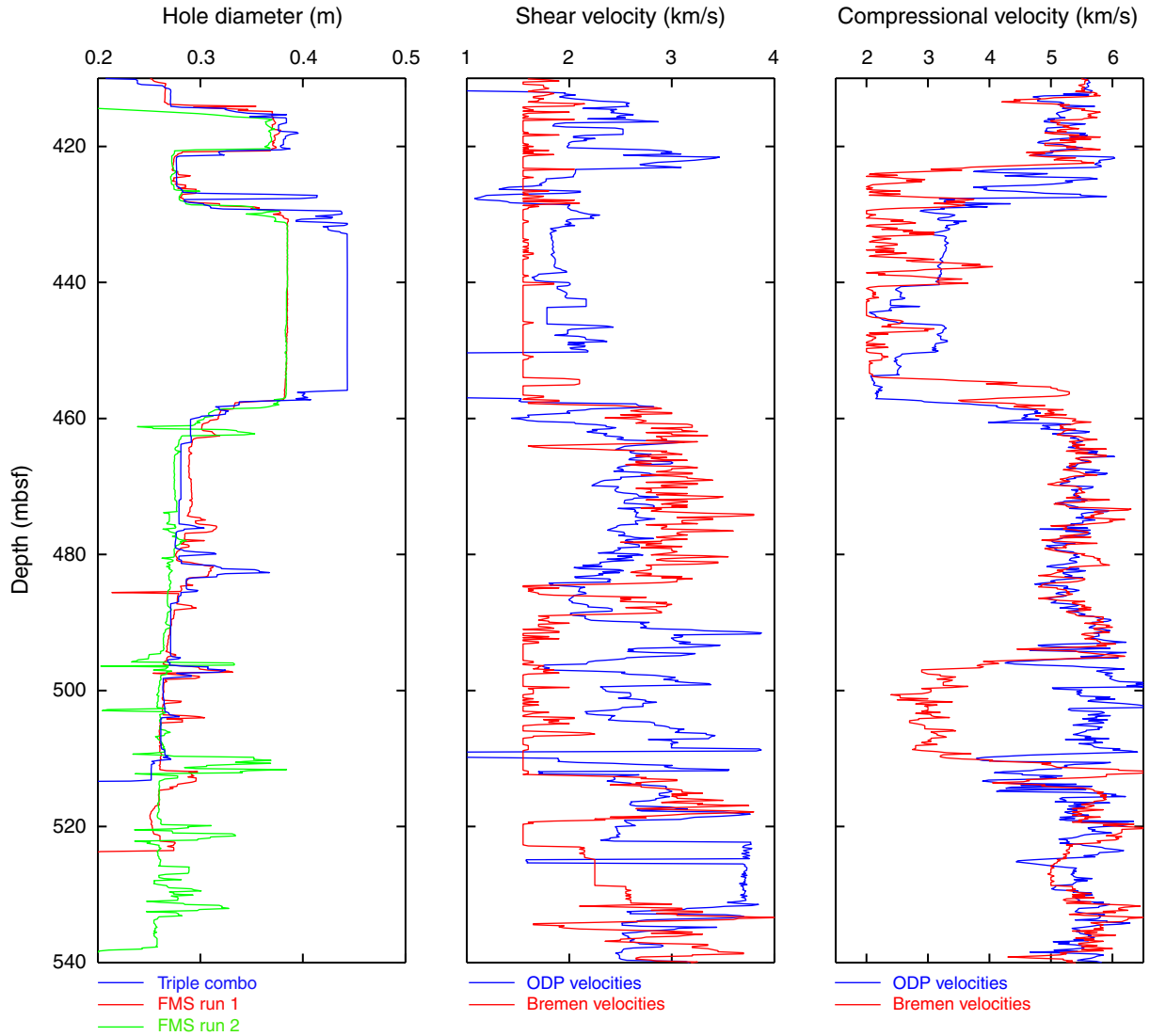
Figure F7. Borehole diameter measurements (left), picked Stoneley wave velocity, and estimate of Stoneley energy (right). Green line = Stoneley velocity approximated for low frequencies. In the igneous section, ODP-picked Stoneley velocities agree very well with ours, indicating a reliably working algorithm. Energy of the Stoneley wave is given in relation to maximum energy measured along the profile (at 405 mbsf) and indicated as energy loss in decibels. FMS = Formation MicroScanner.
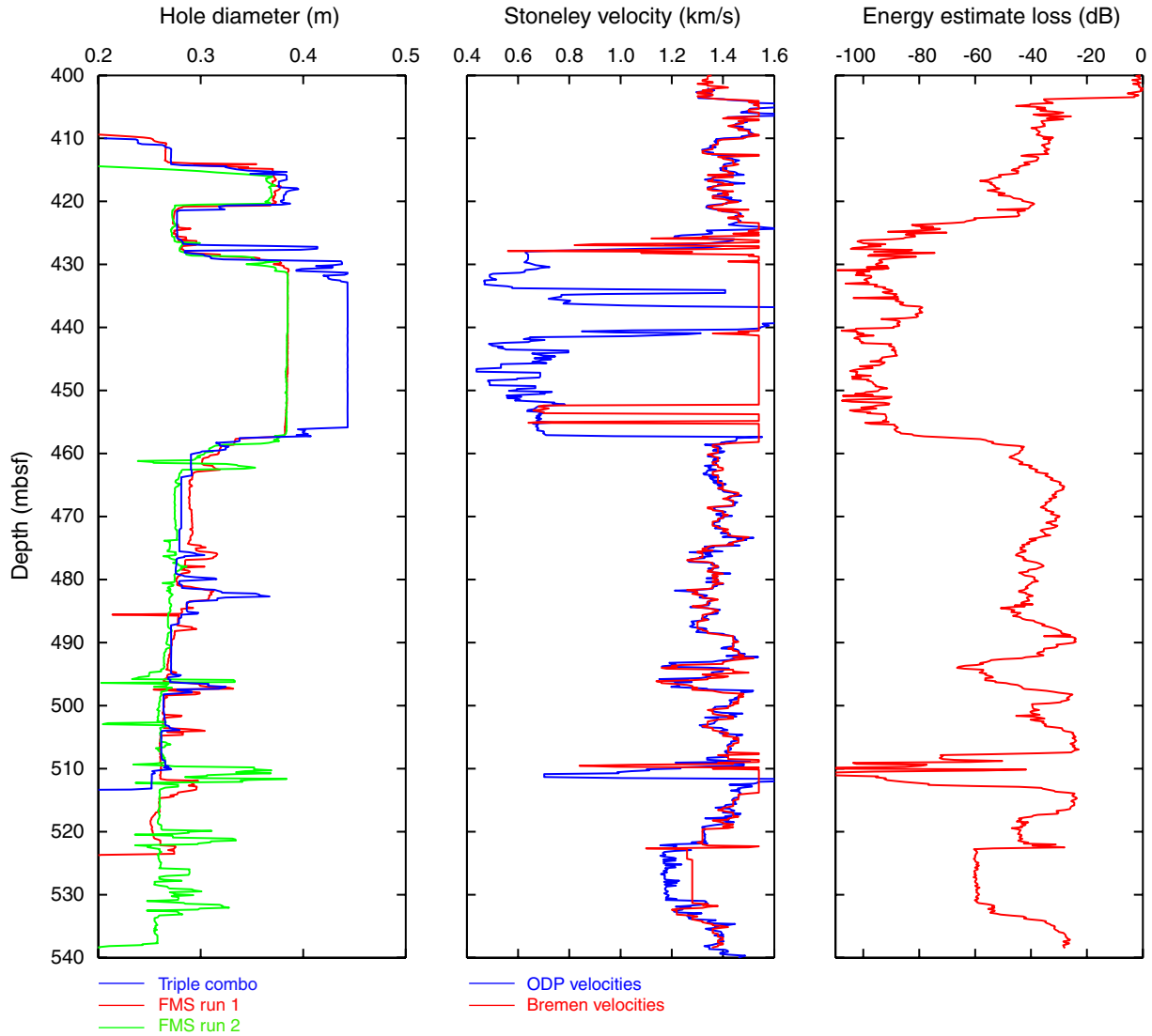
Figure F8. Borehole diameter measurements (left), picked Stoneley wave velocity, and estimate of Stoneley energy (right) in detail. Borehole diameter as determined from the triple combo and FMS tools. Light blue = regions of smooth borehole walls, red arrows = locations of energy losses despite the smooth wall. We compare our results to other measurements that might indicate fracture density, such as fracture observations on cores and geochemical investigations of pore water. Velocity changes are disregarded because data at ~510 mbsf are erroneous and we assume the energy estimate, determined independently from velocity, not to be influenced. FMS = Formation MicroScanner.
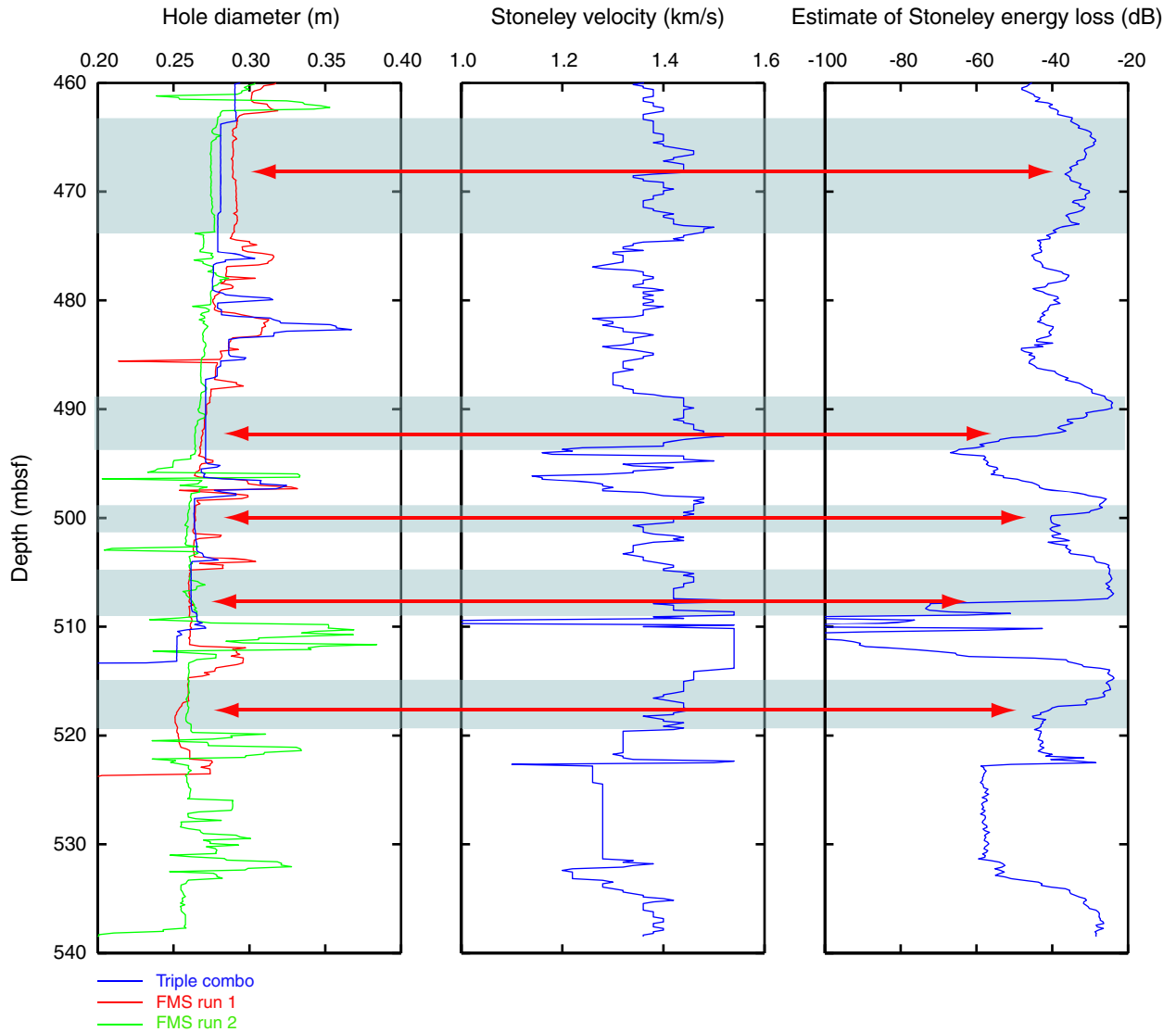
Figure F9. Compilation of core recovery, number of fractures counted on FMS, number of fractures counted on recovered core material, estimate of Stoneley energy and borehole diameter. Light blue = regions of smooth borehole wall, red arrows = energy losses despite the smooth wall. FMS did not deliver reliable data from 510 to 514 mbsf. FMS = Formation MicroScanner.
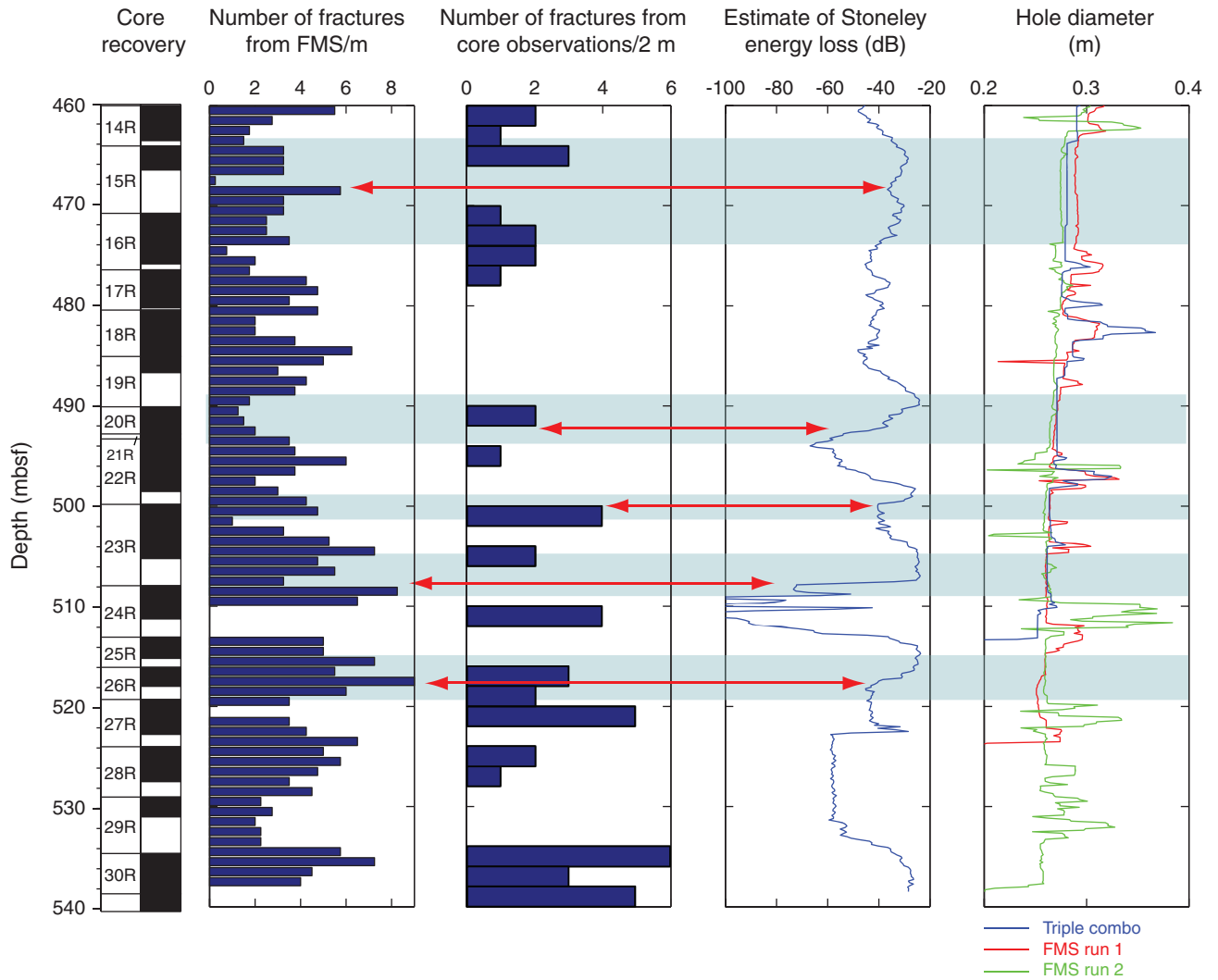
Table T1. Overview of borehole acoustic modes.

Mode	Type	Features	Range of velocity
P and S head waves	Partially reflected compressional and shear waves	Governs compressional and shear head wave	$V_m = V_P$, $V_m = V_S$
P and S normal modes	Fully reflected compressional and shear waves	Fully trapped, dispersive, dominate signal in far field	$V_m < V_P$, $V_m < V_S$, velocity different from formation velocity
Stoneley wave	Interface wave, fundamental mode	Velocity and attenuation depend on formation permeability	$0.75\ V_F < V_m < V_F$

Notes: Adapted from Hearst et al. (2001). V_P = compressional acoustic velocity of the wave spreading in a medium, V_S = shear velocity, V_F = velocity of the waves in the borehole fluid, V_m = velocity of the particular mode.

Table T2. Parameters used in the semblance analysis to calculate velocities (V_P, V_S, and V_{st}) and amplitudes.

Measurement	P- and S-waves	Stoneley waves
Velocity range (m/s)	1550–6600	400–1540
Velocity resolution (m/s)	50	20
Start time (µs)	500–1800	1600–4800
Time resolution (µs)	1	1
Window length	8 samples; 12.5 kHz	40 samples; 625 Hz
Limitations	$V_P/1.4 > V_S > V_F$; variations between shots < 500 m/s	$V_{st} < V_F$

Notes: In P&S mode, the labeling algorithm distinguishes between *P* and *S* head wave arrivals. These limitations are based on physical limitations described in (Kimball and Marzetta, 1984).